AGU PUBLICATIONS

JGR

Journal of Geophysical Research: Space Physics

RESEARCH ARTICLE

10.1002/2014JA020797

Key Points:
- Analytic solution for Free-end modes
- Importance of boundary condition on plasma density estimation
- Improvement over WKB method

Correspondence to:
J. Bulusu,
bulusujayashree@gmail.com

Citation:
Bulusu, J., A. K. Sinha, and G. Vichare (2015), An analytic model of toroidal half-wave oscillations: Implication on plasma density estimates, *J. Geophys. Res. Space Physics*, *120*, doi:10.1002/2014JA020797.

Received 7 NOV 2014
Accepted 25 MAR 2015
Accepted article online 1 APR 2015

An analytic model of toroidal half-wave oscillations: Implication on plasma density estimates

Jayashree Bulusu[1], A. K. Sinha[1], and Geeta Vichare[1]

[1] Indian Institute of Geomagnetism, Navi Mumbai, India

Abstract The developed analytic model for toroidal oscillations under infinitely conducting ionosphere ("Rigid-end") has been extended to "Free-end" case when the conjugate ionospheres are infinitely resistive. The present direct analytic model (DAM) is the only analytic model that provides the field line structures of electric and magnetic field oscillations associated with the "Free-end" toroidal wave for generalized plasma distribution characterized by the power law $\rho = \rho_o(r_o/r)^m$, where m is the density index and r is the geocentric distance to the position of interest on the field line. This is important because different regions in the magnetosphere are characterized by different m. Significant improvement over standard WKB solution and an excellent agreement with the numerical exact solution (NES) affirms validity and advancement of DAM. In addition, we estimate the equatorial ion number density (assuming H^+ atom as the only species) using DAM, NES, and standard WKB for Rigid-end as well as Free-end case and illustrate their respective implications in computing ion number density. It is seen that WKB method overestimates the equatorial ion density under Rigid-end condition and underestimates the same under Free-end condition. The density estimates through DAM are far more accurate than those computed through WKB. The earlier analytic estimates of ion number density were restricted to $m = 6$, whereas DAM can account for generalized m while reproducing the density for $m = 6$ as envisaged by earlier models.

1. Introduction

Many experimental as well as remote sensing techniques are being developed to probe the Earth's magnetosphere. In the last few years ultralow frequency (ULF) waves observed in space are used to estimate ion density in different regions of the magnetosphere, and this technique is termed as magnetospheric seismology [*Guglielmi*, 1974; *Baransky et al.*, 1985; *Guglielmi*, 1989; *Fedorov et al.*, 1990; *Denton et al.*, 2001, 2004; *Chi and Russell*, 2005; *Berube et al.*, 2006; *Takahashi and Denton*, 2007]. The success of the techniques lies in the precise identification of field line frequency and use of appropriate theoretical model incorporating suitable boundary conditions. These ULF oscillations, otherwise termed as geomagnetic pulsations, are small amplitude (few tenths of nT to 100 nT) long period (10 s–1000 s) magnetic field fluctuations observed in ground and space. These oscillations are consequences of Alfvén waves standing on geomagnetic field lines [*Dungey*, 1954]. Under cold plasma approximation, these oscillations can be categorized to shear Alfvén mode and fast compressional mode [*Dungey*, 1968]. The former deals with transverse magnetic field perturbation and energy is guided along field line. The fast mode, on the other hand, has a component along the ambient field and energy moves in the direction of the wave vector, which can make any angle with the ambient field. The background nonuniform magnetic field couples the two modes and has been discussed in different magnetic field geometries by different authors [*Lanzerotti and Southwood*, 1979; *Leonovich*, 2001; *Waters et al.*, 2013]. The coupled equation has not been solved in dipole magnetic field geometry. However, the extreme limit of azimuthal wave number k_ϕ decouples the mode to toroidal ($k_\phi \sim 0$) or poloidal ($k_\phi \sim \infty$) oscillation along with the compressional mode [*Orr*, 1973]. The toroidal and poloidal modes are characterized by azimuthal and meridional magnetic field perturbation, respectively, and often the poloidal mode gets transformed to toroidal in the Earth's magnetosphere [*Leonovich and Mazur*, 1993; *Mann and Wright*, 1995; *Klimushkin et al.*, 2004; *Mager and Klimushkin*, 2006, 2007]. The time scale of this transformation depends on the azimuthal wave number associated with the wave. Theoretical aspects of these oscillations have been discussed by many previous authors [*Radoski*, 1967; *Cummings et al.*, 1969; *McClay*, 1970; *Orr and Mathew*, 1971; *Southwood*, 1974; *Krylov and Fedorov*, 1976; *Newton et al.*, 1978; *Allan and Knox*, 1979a; *Krylov et al.*, 1979, 1980; *Krylov and Lifshitz*, 1984; *Sinha and Rajaram*, 1997; *Ozeke and Mann*, 2005]. There are many observations of these oscillations

[*Cummings et al.*, 1969; *Engebretson et al.*, 1986; *Anderson et al.*, 1990; *Sinha et al.*, 2005; *Bochev and Sinha*, 2010; *Liu et al.*, 2013; *Takahashi et al.*, 2013].

The reflection at the ionosphere plays a crucial role in generating standing wave modes of different wavelengths. This reflection is decided by the balance between the ionospheric Pedersen conductance $\Sigma_P^{N,S}$ and the conductance of Alfvén wave at the conjugate point Σ_A. The superscripts N and S represent the northern and southern conjugate points, respectively, and the wave conductance $\Sigma_A = 1/\mu_0 V_A^c$, where V_A^c is the Alfvén velocity at the conjugate point. The type of the standing wave formed on the field line depends on the sign of the reflection coefficient at the conjugate points. The reflection coefficient at the ionosphere can be computed by $R^{N,S} = \frac{\Sigma_A - \Sigma_P^{N,S}}{\Sigma_A + \Sigma_P^{N,S}}$ given by *Scholer* [1970]. Similar sign of R at the conjugate points gives rise to half-wave modes, whereas a change in sign of the R generates a quarter-wave mode. According to *Hughes and Southwood* [1976], the half waves are further classified into two types described as follows. (1) The ionosphere is infinitely conducting at both hemispheres (i.e., $\Sigma_P^{N,S} > \Sigma_A$ a typical condition for a half-wave), the electric field as well as the wave displacement must vanish at the foot of the field lines at the conjugate ionospheres leading to the "Rigid-end mode." The reflection coefficient $R^{N,S}$ must follow the relation $R^{N,S} < 0$ at both conjugate points. (2) The ionospheric conductivity is vanishingly small at both hemispheres (i.e., $\Sigma_P^{N,S} < \Sigma_A$ condition favorable for local midnight during equinoxes: again a typical condition for a half-wave), the magnetic field vanishes at the foot of the field lines at the conjugate ionospheres, whereas the electric field and wave displacement still have a finite value leading to a "Free-end mode." In this case, $R^{N,S} > 0$ at both conjugate points. The Rigid-end and Free-end conditions of half-wave mimic the local noon and midnight during equinoxes, respectively. There exists another special standing Alfvén wave, termed as quarter wave, formed under extremely asymmetric ionospheric boundary condition at the conjugate points [*Allan and Knox*, 1979a, 1979b]. These waves are dominant around dawn and dusk MLT hours during solstices. The spatial and temporal characteristics of these waves in comparison to half waves are thoroughly discussed very recently by *Bulusu et al.* [2014].

It is to be noted that the terms half and quarter waves mentioned above represent the relation of wavelength of oscillation to the scale size of the system for the fundamental. When the scale size of the system is half of the wavelength of standing wave, it is termed as half-wave, and when the scale of the system is one fourth of the wavelength, it is termed as quarter wave.

The first analytic picture of the toroidal oscillations was presented by *Warner and Orr* [1979]. They used the *Mead and Fairfield* [1975] model of the magnetosphere and computed the time of flight between the two conjugate ionospheres by using the WKB method. The fundamental period obtained using WKB method showed large departure as regard to the time period of the wave. This departure was attributed to the breaking down of WKB method for the fundamental as the wavelength of oscillation is comparable to the scale size of the system [*Singer et al.*, 1981]. This implies that for higher harmonics, the departure in WKB frequency from the numerical exact frequency should be negligibly small. However, *Sinha and Rajaram* [1997] showed that the departure in the frequency got saturated with increasing harmonic number and did not vanish even for the harmonic as large as 20. They attributed this discrepancy to the inability of the WKB method in handling the singularities at the turning points (colatitude $\theta \sim 0$ and $\theta \sim \pi$). They could obtain a natural and self-consistent analytic solution for Rigid-end toroidal eigenmodes in the dipole field geometry by ensuring that the solution was well behaved at the turning points.

All the previous work mentioned so far assumed the ionosphere to be infinitely conducting. The problem of the Free-end modes was first envisaged by *Newton et al.* [1978]. Thereafter, characteristics of these modes were studied by various authors in different field geometries [*Allan and Knox*, 1979a, 1979b; *Allan*, 1983; *Southwood and Kivelson*, 1990; *Sinha and Rajaram*, 2003; *Ozeke and Mann*, 2005]. The analytic formalism prescribed by *Allan and Knox* [1979a, 1979b] and *Ozeke and Mann* [2005] were restricted only to the density variation of $1/r^6$ along the field line. It is important to get an analytic solution for Rigid-end as well as Free-end for different density variations as different magnetospheric regions follow different density variations along the field line [*Carpenter and Smith*, 1964; *Newbury et al.*, 1989; *Gallagher et al.*, 2000; *Goldstein et al.*, 2001]. The analytic solution for Rigid-end was put forth by *Sinha and Rajaram* [1997] for generalized density distribution in the dipole field geometry. They discussed the importance of analytic solution over WKB solution. Here we reproduce the analytic solution for Rigid-end and extend the model to get an analytic solution for Free-end toroidal oscillations. The Free-end solution along with the Rigid-end solution can provide the estimation of ion number densities for ULFs observed in any local time sector.

Conventionally, the estimation of the ion number densities are carried out under the assumption of infinitely conducting ionospheric boundary conditions, i.e., Rigid-end condition [*Denton et al.*, 2001, 2004; *Takahashi and Denton*, 2007; *Min et al.*, 2013]. This will cause an error in the estimation as an assumption of infinitely high conducting ionosphere is appropriate for the events during daytime only. Estimates of such errors are discussed by *Ozeke and Mann* [2005]. They addressed the departure in the densities obtained from Rigid-end and Free-end cases for the same observed frequency and showed the errors that can occur in numerical, analytic, and WKB method. However, their analytic model could account only for a density variation of $1/r^6$ type along the field line. For density variation other than $1/r^6$ along the field line, the WKB approach was suggested. However, as mentioned earlier, *Sinha and Rajaram* [1997] showed that the WKB frequencies depart significantly from the exact frequencies especially for lower harmonics which are mostly observed and are used for density estimation. This implies that ion number density obtained from WKB method would also depart significantly from that estimated through exact solution. This aspect is addressed in this paper in detail along with the development of an analytic model for Free-end half-wave in dipole field for generalized plasma distribution. For the sake of completion we also discuss the analytic Rigid-end solution in context with the conventional estimation of ion number density. The paper is organized as mentioned in the following paragraph.

Section 2 describes the general theoretical background of analytic model of toroidal half waves. In section 2.1 we reproduce the direct analytic model (DAM) for the Rigid-end given by *Sinha and Rajaram* [1997] and extend it for Free-end toroidal mode. In section 2.3, we present the numerical exact solution (NES) for the Rigid-end and Free-end so as to compare the results with corresponding analytic solutions. Validity of assumptions is examined in section 3. The temporal and spatial characteristics of the toroidal eigenmodes for Rigid-end and Free-end are discussed in section 4. The importance of boundary condition in estimating ion number densities along with a comparative account of different methods (DAM, NES, and WKB) are illustrated in section 5. Conclusions are included in section 6.

2. Theoretical Background

In generalized curvilinear orthogonal coordinate system, *Singer et al.* [1981] described the long-period transverse waves in cold, infinitely conducting, and stationary magnetized plasma in a single exact linear wave equation as

$$\mu_o \rho \frac{\partial^2}{\partial t^2}\left(\frac{\xi_\alpha}{h_\alpha}\right) = \frac{1}{h_\alpha^2}\vec{B_o}.\vec{\nabla}\left[h_{\alpha^2}\vec{B_o}.\vec{\nabla}\left(\frac{\xi_\alpha}{h_\alpha}\right)\right] \tag{1}$$

where μ_o is the magnetic permeability in vacuum, ρ is plasma mass density, ξ_α is the plasma displacement perpendicular to the field line, $\vec{B_o}$ is the ambient magnetic field direction; the parameter α determines the mode of oscillation, and its direction $\vec{\alpha}$ signifies the plasma displacement. The parameter h_α is the scale factor for the normal separation between the field lines in the direction of $\vec{\alpha}$ and is determined by the magnetic field geometry. The associated electric and magnetic field structures can be obtained using the following equations.

$$b_\alpha = h_\alpha B_o \frac{\mathrm{d}}{\mathrm{d}S}\left(\frac{\xi_\alpha}{h_\alpha}\right) \tag{2}$$

$$E_\beta = \omega \xi_\alpha B_o \tag{3}$$

where $(\vec{B_0}/B_0, \vec{\alpha}, \vec{\beta})$ form the right-handed orthogonal system.

The versatility of the above equation is seen from its applicability to both dipolar and nondipolar magnetic field geometry, and this equation can be solved for uncoupled toroidal and poloidal oscillations in general. If s denotes the distance along the field line from the equator, ϕ denotes the longitude, and ν denotes the meridional distance then $(\hat{s}, \hat{\phi}, \hat{\nu})$ form a right-handed orthogonal system where $\hat{s} = \frac{\vec{\nabla} s}{|\nabla s|}$, $\hat{\phi} = \frac{\vec{\nabla}\phi}{|\nabla \phi|}$, and $\hat{\nu} = \hat{s} \times \hat{\phi}$. For toroidal oscillation α and β correspond respectively to ϕ and ν, whereas for poloidal oscillation they respectively correspond to ν and ϕ.

For infinitely conducting ionospheric boundaries (Rigid-end), analytic as well as numerical solutions to equation (1) for toroidal oscillations were developed by *Sinha and Rajaram* [1997] in the dipole field geometry. In the present study, we extend the analysis to examine the spatial and temporal characteristics of toroidal oscillations for insulating ionospheres (Free-end) by making the necessary changes in the ionospheric boundary conditions. The solution for Rigid-end is also reproduced for the sake of comparison.

2.1. Direct Analytic Method (DAM) for Toroidal Oscillations

We solve equation (1) under the following assumptions.

1. The background magnetic field is dipolar;
2. Perturbed quantities vary as $\exp[i\omega\tau]$;
3. Density variation is governed by the power law $\rho = \rho_o(r_o/r)^m$,

where m is the density index and ρ_o is proton mass density at r_o, the geocentric distance to equatorial crossing point of the field line considered, and r is the geocentric distance to the position of interest on the field line.

With the assumption that the background magnetic field is dipolar, the parameters h_α, B_0, and equatorial magnetic field $B_{\rm eq}$ are given by the following expressions: $h_\alpha = L\sin^3\theta$ for the toroidal mode, $B_0 = B_{\rm eq}\sqrt{1+3\cos^3\theta}/\sin^6\theta$, and $B_{\rm eq} = 0.311\times10^{-4}/L^3$ Tesla. Here $L = 1/\sin^2\theta_c$ (suffix c indicates the value at the conjugate point and θ)is the colatitude and is the geocentric distance (in Earth radius, R_E), of the point where the field line crosses the equator.

Sinha and Rajaram [1997] discussed how the turning points ($\theta \sim 0$ or π) affect the solution for Rigid-end case. Adopting the identical formalism as in *Sinha and Rajaram* [1997], the mode equation (1) can be written as

$$\epsilon^2\frac{{\rm d}^2X}{{\rm d}v^2} + \Phi(v)X = 0 \tag{4}$$

where $\epsilon = 1/L^2$, $X = \frac{\xi_\alpha}{R_E h_\alpha}$, $S = \frac{s}{R_E}$, $\frac{{\rm d}v}{{\rm d}S} = \frac{B_{\rm eq}}{h_\alpha^2 B}$, $\Omega = \frac{\omega R_E}{V_{\rm Aeq}}$, $\Phi(v) = \Omega^2\sin^{2r}\theta$, $r = 6-m$, and $V_{\rm Aeq} = \frac{B_{\rm eq}}{\mu_0\rho_0}$. $V_{\rm Aeq}$ is the Alfvén velocity at the equator and X is the normalized displacement along the field line. The independent variable v in equation (4) can be explicitly written as $v = \frac{1\pm\cos\theta}{L}$, where the minus and plus signs denote the Northern and Southern Hemispheres, respectively. It should be noted that equation (4) becomes singular when $\Phi(v) = 0$, i.e., at $\theta = 0, \pi$. The singularity is handled mathematically by using the methodology of *Langer* [1949].

By making the transformations $X = a(v)Z$, $a(v) \neq 0$, $\zeta = \zeta(v)$, $a(v) = ({\rm d}\zeta/{\rm d}v)^{-1/2}$, and $\zeta^r({\rm d}\zeta/{\rm d}v)^2 = \Phi(v)$, equation (4) takes the form

$$\left[\frac{{\rm d}^2}{{\rm d}\zeta^2} + \frac{\zeta^r}{\epsilon^2} + a^3\frac{{\rm d}^2a(v)}{{\rm d}v^2}\right]Z = 0 \tag{5}$$

If we neglect the last term in equation (5) (justified in section 3), it gets transformed to the standard Bessel equation

$$\frac{{\rm d}^2u}{{\rm d}\eta^2} + \frac{1}{\eta}\frac{{\rm d}u}{{\rm d}\eta} + \left[1-\frac{\nu^2}{\eta^2}\right]u = 0 \tag{6}$$

where $\eta = (2/\epsilon)\zeta^{r+2/2}/(r+2)$, $Z = \sqrt{\zeta}u$, and $\nu = 1/(r+2)$. Equation (6) is solved in two hemispheres, and it is ensured that the solution is analytically continuous by matching the solution and its derivative at the equator. It should be noted that $\eta = \frac{\omega LR_E}{V_{\rm Aeq}}\int_0^\theta \sin^{7-m}\theta$ for the Northern Hemisphere, and $\eta = \frac{\omega LR_E}{V_{\rm Aeq}}\int_\theta^\pi \sin^{7-m}\theta$ for the Southern Hemisphere. Thus, the solution of equation (4) in terms of normalized displacement X can be written as

$$X = \sqrt{\frac{1}{2L\nu}}\sqrt{\frac{V_{\rm Aeq}}{\omega LR_E}}\frac{\eta^{1/2}}{\sin^{3-m/2}\theta}\left[J_\nu(\eta) + KJ_{-\nu}(\eta)\right] \tag{7}$$

where, $J_\nu(\eta)$ and $J_{-\nu}(\eta)$ are Bessel functions of the first kind in the variable η and of order ν and $-\nu$, respectively. The arbitrary constant K in equation (7) is determined by using appropriate boundary conditions relevant either to "Rigid-end" or to "Free-end" modes. Thus, the field line structures of toroidal half-wave modes are obtained in a complete analytic form for a generalized plasma distribution in a dipolar field geometry. We call this method as DAM (Direct Analytic Method).

2.2. Ideal Boundary Conditions (Rigid-End and Free-End Cases)

To determine arbitrary constant K of solution (7), Rigid-end (Free-end) boundary condition, we impose $X = 0$ (${\rm d}X/{\rm d}S$=0). Thus, the solution for Rigid-end and Free-end can be explicitly written by putting the appropriate value of K in equation (7), i.e.,

$$K = -[J_\nu(\eta)/J_{-\nu}(\eta)]_{\theta=\theta_c} \tag{8}$$

for Rigid-end and

$$K = \left[\frac{\left[\left(\frac{3-m/2}{L\tan\theta\Omega(\mathrm{d}\eta/\mathrm{d}\theta)} - \frac{1}{2\eta} \right) J_\nu(\eta) - J'_\nu(\eta) \right]}{\left[J'_{-\nu}(\eta) - \left(\frac{3-m/2}{L\tan\theta\Omega(d\eta/d\theta)} - \frac{1}{2\eta} \right) J_{-\nu}(\eta) \right]} \right]_{\theta=\theta_c} \tag{9}$$

for Free-end.

Analytic continuation of X and $\frac{\mathrm{d}X}{\mathrm{d}S}$ at the equator ensures that either the solution or its derivative vanishes at the equator, which is a natural condition for even and odd harmonics, respectively, for the Rigid-end condition. However, for the Free-end case the solution should vanish for odd harmonics at the equator, whereas vanishing derivative at the equator is the natural condition for even harmonics. Thus, using the above condition on the solution along with its derivative, the eigenfrequencies are determined in a natural and self-consistent way.

2.3. Numerical Exact Solution (NES) for Toroidal Oscillations

The mode equation (1) is solved numerically using second-order Runge-Kutta method and the exact frequency is obtained by shooting method using the appropriate boundary conditions that either the eigenfunction X (for Rigid-end case) or its derivative $\frac{\mathrm{d}X}{\mathrm{d}S}$ (for Free-end case) must vanish at the ionosphere. Even and odd harmonics are decided by imposing the condition at the equator. For Rigid-end case the solution (its derivative) vanishes at the equator for even (odd) harmonics. The equatorial condition is reversed for Free-end case. Once the frequency is determined, the solution and its derivative could be obtained by solving the normalized equation. This method of numerical solution is referred as Numerical Exact Solution (NES).

3. Validity of Neglecting the Last Term in Equation (5)

3.1. On Analytic Grounds

In order to understand the importance of each term of equation (5), the variation of each term with respect to L and m was examined. It is seen that the first term varies as L^2 and is independent of density index m. The second term varies as $L^{2(3r+4)/(r+2)}$. For extreme values of m as 0 and 6, the L dependence of the second term is, respectively, $L^{5/2}$ and L^4. However, the dependence of the third term on L and m is very different. For density indices between $m = 0$ and $m = 5$, the third term $(a^3 \frac{\mathrm{d}^2}{\mathrm{d}v^2} a(v))$ varies as $L^{-2(r-2)/(r+2)}$ with respect to L. For $m = 6$ this term vanishes. For $m = 0$–5, the ratio of the first term to the third term is proportional to $L^{4r/(r+2)}$ and the ratio of the second term to the third term is proportional to $L^{4(2r+1)/(r+2)}$. This shows the significant dominance of the first two terms over the third term. It should be noted that for $L > 1$, the third term can be neglected. However, with increasing L, the third term becomes increasingly insignificant. Depending on the variation of each term with respect to L and m of equation (5), and considering the ratios between the terms, it is justified to neglect the third term on physical grounds.

3.2. On Numerical Grounds

Neglecting the last term in equation (5) is tantamount to adding $(-\frac{\epsilon^2}{a}\frac{\mathrm{d}^2 a}{\mathrm{d}v^2}X)$ in the left-hand side of equation (4) resulting into

$$\epsilon^2 \frac{\mathrm{d}^2 X}{\mathrm{d}v^2} + v^r \Psi(v) X - \frac{\epsilon^2}{a}\frac{\mathrm{d}^2 a}{\mathrm{d}v^2} X = 0 \tag{10}$$

Equation (10) was exactly solved for X using the second-order Runge-Kutta method for both the Rigid-end and Free-end cases. Results thus obtained were compared with the numerical exact solution of equation (4) as explained in section 2.3. The comparison has been shown in Figure 1, where index 1 represents the solution of equation (10), i.e., after neglecting the last term in equation (5), and the index 2 represents the solution of equation (4), i.e., considering all terms. In terms of physical quantities, normalized plasma displacement (X) is proportional to the electric field associated to the toroidal oscillations, whereas $Y(= h_\alpha^2 B \frac{\mathrm{d}X}{\mathrm{d}S})$ is proportional to the magnetic field associated with these oscillations. Figures 1 (top left) and 1 (top right) denote the field line structure of X and Y, respectively for Rigid-end case and Figures 1 (bottom left) and 1 (bottom right) denote these parameters for Free-end case.

The analysis was performed for different values of density index, and as expected the departure was maximum for $m = 0$ when the effect of singularity is maximum as is evident from the term $\Phi(v)$. Even for the worst case of $m = 0$, the maximum departure in X for Rigid-end and Free-end cases was, respectively, 3% and 2%. The

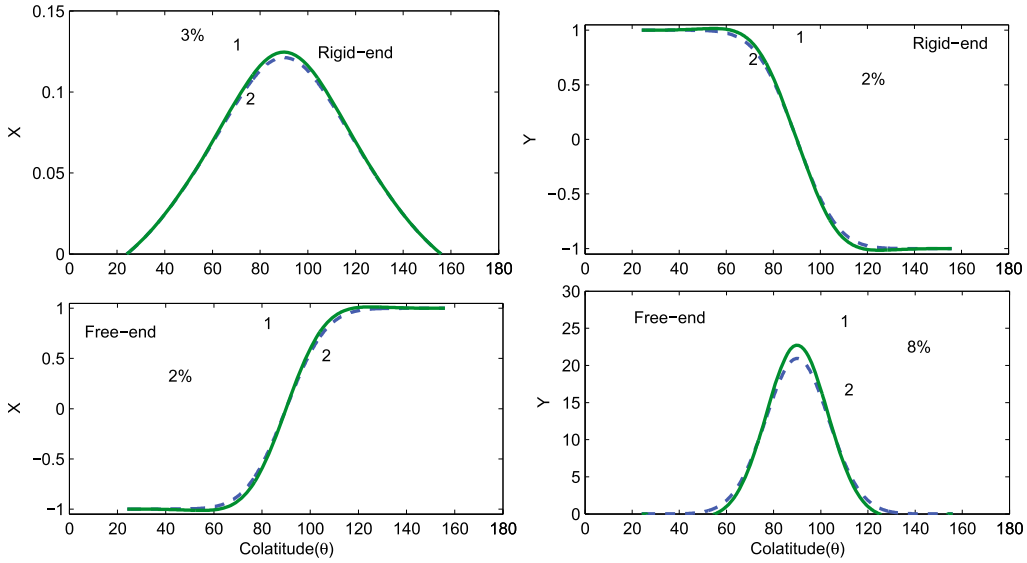

Figure 1. The plots of X (related to electric field) and Y (related to the derivative of X, associated with magnetic field) for $m = 0$ as a function of colatitude of θ for (top row) Rigid-end and (bottom row) Free-end. Index 1 represents the solution of equation (10) and index 2 represents the solution of equation (4).

maximum departure in Y for Rigid-end and Free-end cases was found to be 2% and 8%, respectively. These small departures in X and Y computed through equations (10) and (4) justifies neglecting the last term in square bracket of equation (5).

4. Results and Discussions

4.1. Temporal Behavior for Idealized Ionospheric Conductivity

This section discusses the temporal characteristics of toroidal oscillations in the extreme limits of ionospheric conductivities. The eigenperiods and eigenfrequencies are computed for equatorial proton density of 1/cm^3. The fundamental and second harmonic frequencies are estimated for a range of density indices from $m = 0$–4 at $L = 6.6$ using three discussed methods, i.e., WKB, DAM, and NES. ω_{WKB} denotes the frequency obtained by WKB method, whereas ω_D^R and ω_D^F denote the frequencies obtained through DAM for Rigid-end and Free-end cases, respectively. ω_E^R and ω_E^F are the frequencies for Rigid-end and Free-end cases, respectively, using NES method. The percentage departure in frequencies obtained using DAM from that obtained using NES are shown in Table 1. It is seen that as the density index m increases, the percentage departure in frequency computed using DAM from the exact frequency $\left[\frac{(\omega_D^R-\omega_E^R)}{\omega_E^R}\times 100\right]$ and $\left[\frac{(\omega_D^F-\omega_E^F)}{\omega_E^F}\times 100\right]$, respectively, for Rigid-end and Free-end, decreases for both fundamental and the second harmonic. The maximum departure is only 16.5% and 7% for fundamental Rigid-end and Free-end, respectively, for the worst case of $m = 0$ when the effect of singularity on the solution is maximum. Also, the frequencies estimated using DAM and NES for higher values of density indices are in good agreement for both Rigid-end and Free-end cases.

This is a remarkable improvement over the formal WKB frequency, which departs 60% and 26% respectively for fundamental Rigid-end and Free-end, from the exact frequency (shown as $\left[\frac{(\omega_{\mathrm{WKB}}-\omega_E^R)}{\omega_E^R}\times 100\right]$ and $\left[\frac{(\omega_E^F-\omega_{\mathrm{WKB}})}{\omega_{\mathrm{WKB}}}\times 100\right]$) for $m = 0$ (Table 2). It is important to note that the WKB frequency, computed using time of flight, does not distinguish between Rigid-end and Free-end.

Figure 2a represents the fundamental frequency obtained analytically (using DAM) for Rigid-end and Free-end along with WKB frequency for density index $m = 0$ at $L = 6.6$. Emphasis has been given to $L = 6.6$, because this corresponds to the geostationary satellite, though this analysis holds good for any value of L. It can be seen that the frequency for Rigid-end is smaller compared to WKB and that for Free-end is greater than the WKB frequency. This feature is predominant specially in case of the fundamental. As the harmonic number is increased, the frequency obtained from all the three approaches converges. This result is on the expected line, as WKB solution breaks down mainly for the fundamental and the lower harmonics where the

Table 1. Percentage Departure of Toroidal Frequencies Estimated Using Direct Analytic Method (DAM) From Corresponding Numerical Exact Solution (NES) for Rigid-End and Free-End Cases at $L = 6.6$

Density Index	Harmonic Number	% Departure of ω_D From ω_E	
m	HN	$\frac{(\omega_D^R-\omega_E^R)}{\omega_E^R}\times 100$	$\frac{(\omega_D^F-\omega_E^F)}{\omega_E^F}\times 100$
6	1	0	0
6	2	0	0
5	1	2.1	0.9
5	2	0.28	0.2
4	1	6	3
4	2	0.3	0.33
3	1	8	4
3	2	1	1
2	1	11.5	6
2	2	1.5	1.5
1	1	14	6.5
1	2	2	1.6
0	1	16.5	7
0	2	2.5	2

wavelength of oscillations is comparable to the scale size of the system. In addition, the WKB method does not distinguish between Rigid-end and Free-end conditions. It should be noted that in the present study we take the typical value of density as 1/cm^3 and thus the estimated frequencies fall in the Pc4 range for the geostationary height. If we take the realistic value of proton number density, i.e., in the range 5–10/cm^3, (cf. Figure 5), the frequency falls in the range of Pc5 pulsations which are prevalent at geostationary height [*Takahashi et al.*, 2002; *Takahashi and Denton*, 2007]. The importance of using correct plasma density to reproduce the observed frequency has been emphasized by earlier works [*Sinha et al.*, 2005; *Engebretson et al.*, 1986].

Figure 2b shows the variation of fundamental period with density index m at $L=6.6$. It was seen that for $m = 0$, the departure in fundamental period obtained analytically for the Rigid-end and Free-end from that obtained using WKB are 37% and 35%, respectively. For $m = 6$ (i.e., when plasma density varies as $1/r^6$), fundamental eigenperiod estimated from WKB matches with that obtained for both Rigid-end and Free-end. The periods gradually converge with increasing m and coincide for $m = 6$. This is understandable because for this value of m, the singularity in the term $\Phi(v) = \Omega^2 \sin^{12-2m}\theta$ disappears reducing the problem to that of vibration on a uniform string. As m decreases, the effect of singularity starts affecting the solution and, hence, the estimated period using DAM for Rigid-end and Free-end depart significantly from corresponding WKB period. The present DAM method is an improvement over the formal WKB method in the sense that the singularity is handled properly.

Table 2. Percentage Departure of Toroidal Frequencies Estimated Using WKB Method From Corresponding Numerical Exact Solution for Rigid-End and Free-End Cases at $L = 6.6$

Density Index	Harmonic Number	% Departure of ω_{WKB} From ω_E	
m	HN	$\frac{(\omega_{WKB}-\omega_E^R)}{\omega_E^R}\times 100$	$\frac{(\omega_E^F-\omega_{WKB})}{\omega_{WKB}}\times 100$
6	1	0	0
6	2	0	0
5	1	12.8	12.3
5	2	4.8	6.5
4	1	25	18
4	2	10	10
3	1	35	22
3	2	13	12.5
2	1	45	24
2	2	17	14
1	1	53	25
1	2	19	14.6
0	1	60	26
0	2	21	15

Figure 2c depicts the change in the fundamental eigenperiod over a range of magnetic shells ($L=4-9$) for a typical density index $m=4$. Physically, as the L value is increased, the length of the field line increases and, hence, is the increase in the fundamental period (time for the wave to travel from one conjugate ionosphere to another and back). This is clearly evident from Figure 2c.

4.2. Field Line Structures in the Extreme Limits of Ionospheric Conductivity

The field line structures of electric and magnetic fields associated with the fundamental of toroidal mode for both Rigid-end and Free-end cases are shown in Figure 3, whereas the structures for second harmonic have been shown in Figure 4. Although these structures can be obtained for all values of density index $m = 0-6$, the results presented here are for typical values of $m = 4$ and $L = 6.6$.

4.2.1. Fundamental Mode Structure for Rigid-End and Free-End Cases

Field line structures of electric and magnetic fields along the field lines depend on the iono-

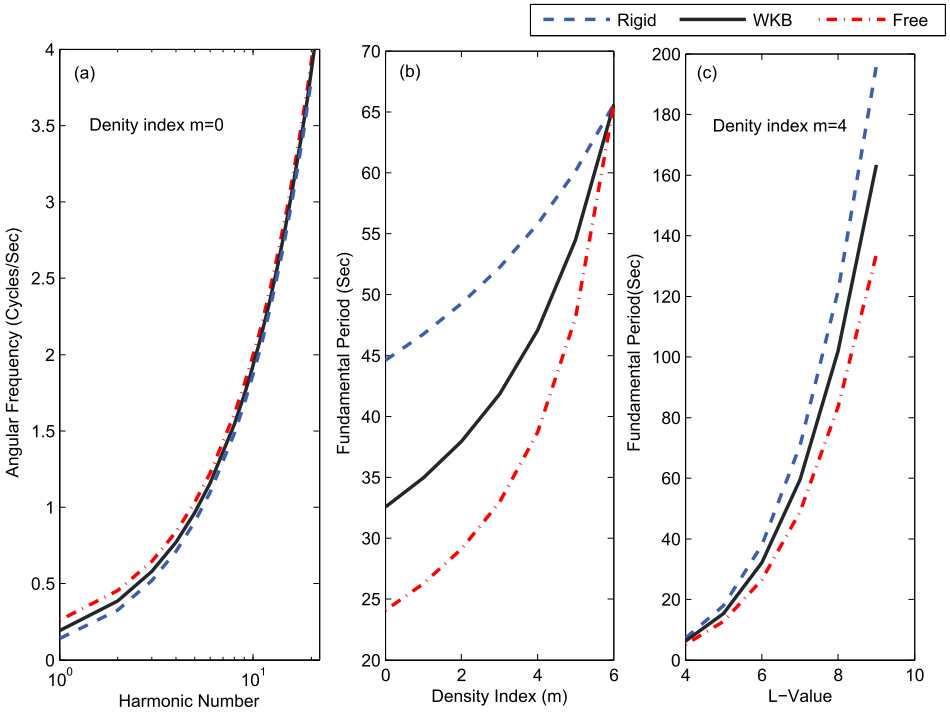

Figure 2. Temporal characteristics of toroidal field line oscillations. Frequencies (Periods) for Rigid-end and Free-end conditions are estimated through DAM and are compared with those computed through WKB. The equatorial proton number density is considered as 1/cm^3. (a) Variation of fundamental frequency with harmonic number for $L = 6.6$ and density index $m = 0$. (b) Variation of fundamental period with density index m for $L = 6.6$. (c) Variation of fundamental period with L value for typical density index $m = 4$.

spheric conductivities at the conjugate points as well as on the harmonic number. For the Rigid-end, the ionosphere is infinitely conducting at conjugate ionospheres. This makes the field displacement negligible at the foot of the field line and thus the electric field sees a node at the conjugate points (Figure 3a). However, the finite current flowing at the conjugate ionospheres result in the antinodes of magnetic field (Figure 3c). In addition, the electric field has an antinode for the fundamental and all the odd harmonics at the equator, whereas the magnetic field is characterized by a node at this point for the Rigid-end. The computed electric and magnetic field variations by DAM match very well with the earlier numerical results of *Cummings et al.* [1969].

For the Free-end, the ionospheric conductivity is negligibly small and thus the current flowing at the conjugate points will be small, resulting in the node formation for the magnetic field at the conjugate points and formation of antinode for the electric field at those points. Figures 3b and 3d show the fundamental electric and magnetic fields, respectively, for Free-end. It is seen that at the equator, the Free-end fundamental and all the odd harmonics of magnetic field result in the formation of antinodes, whereas the corresponding electric field variations show nodes at the equator. In these plots, B_{Surface} and E_{Surface} represent, respectively, the magnetic and electric field fluctuations at the foot of the field line in the ionosphere and T is the wave period.

In this figure, results from DAM and NES are put together for comparison. It can be seen that the solutions obtained from DAM match very well (departure is 2.5% for the fundamental at the equator).

4.2.2. Second Harmonic Spatial Structure for Both Rigid-End and Free-End

The second harmonic and all even harmonics of electric field show a node at the equator along with the nodes at the conjugate points for Rigid-end, and the magnetic field has antinodes at the equator and at both the conjugate points (Figures 4a and 4c). However, the even harmonics of Free-end electric field result in the formation of antinodes at the equator along with the antinodes at the conjugate points (Figure 4b). The second harmonic and all even harmonics of Free-end magnetic field result in the formation of nodes at the equator along with the nodes at the conjugate points (Figure 4d).

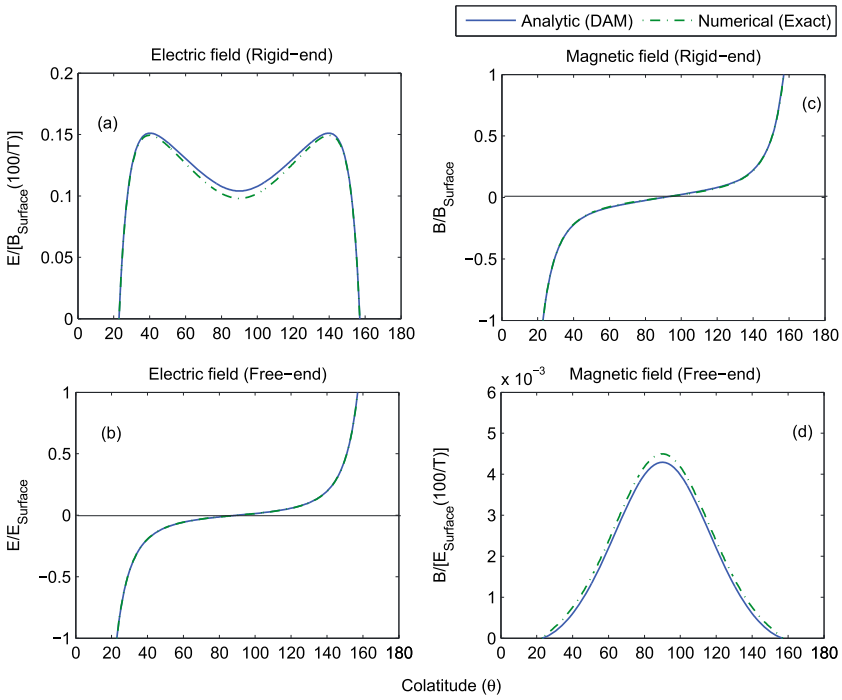

Figure 3. Latitudinal structures of fundamental electric and magnetic fields in Rigid-end and Free-end cases for $m = 4$ and equatorial density is the same as in Figure 2. Shown is the fundamental electric field along the field line for (a) Rigid-end and (b) Free-end. Similarly, also shown is the fundamental magnetic field along the field line for (c) Rigid-end and (d) Free-end. The magnitude of electric field or magnetic field at any point can be obtained by multiplying with the indicated factor. E_{Surface} and B_{Surface} represent the value of electric and magnetic fields, respectively, at the conjugate points. T is the wave period.

At a particular latitude, the electric field fluctuation in mV/m can be obtained by multiplying with the factor ($B_{\text{Surface}}[100/T]$), where T is the wave period for the Rigid-end. However, for the Free-end, the variation of electric field is presented as the fluctuation in the electric field for 1 mV/m electric field variation at the foot of the field line. The variation of the magnetic field in case of Rigid-end is presented as the fluctuation in the magnetic field for 1 nT magnetic field variation at the foot of the field line. At a particular latitude the magnetic field fluctuation for Free-end in nT can be obtained by multiplying the ordinate with $E_{\text{Surface}}[100/T]$.

A comparative study as depicted by Figure 4 shows that there is no departure in the electric and magnetic fields for second and higher harmonics when computed by DAM and NES methods. It is seen that the departure in fundamental frequency of 3% between DAM and NES (refer the estimates for $m = 4$ from Table 1) leads to a departure of only 2.5% in the magnetic fields for Free-end (Figure 3d). On the other hand, the departure in frequency of 0.33% (Table 1) for second harmonic does not reflect any departure in the field-aligned structures of electric and magnetic fields (Figure 4). This puts our analytic model (DAM) on a firmer ground. However, unlike the spatial structures of electric and magnetic fields, the equatorial ion number density is very sensitive even to the slightest change in frequency. The methods for identification of frequencies with minimum error and estimation in equatorial ion number is discussed by *Denton et al.* [2001] and *Takahashi and Denton* [2007]. The use of appropriate boundary condition while estimating the equatorial ion number density is also equally important and is discussed in the following section.

5. Equatorial Ion Number Density Through DAM, NES, and WKB Methods

It is of paramount importance to estimate the ion number densities in different magnetospheric regions in order to probe the Earth's magnetosphere. Magnetospheric seismology is one of the remote sensing techniques developed to estimate the ion number densities using the pulsation frequencies observed by different magnetic and electric field measurements in space [*Takahashi and Denton*, 2007]. Using our theoretical model, we compute ion number densities at different L shells.

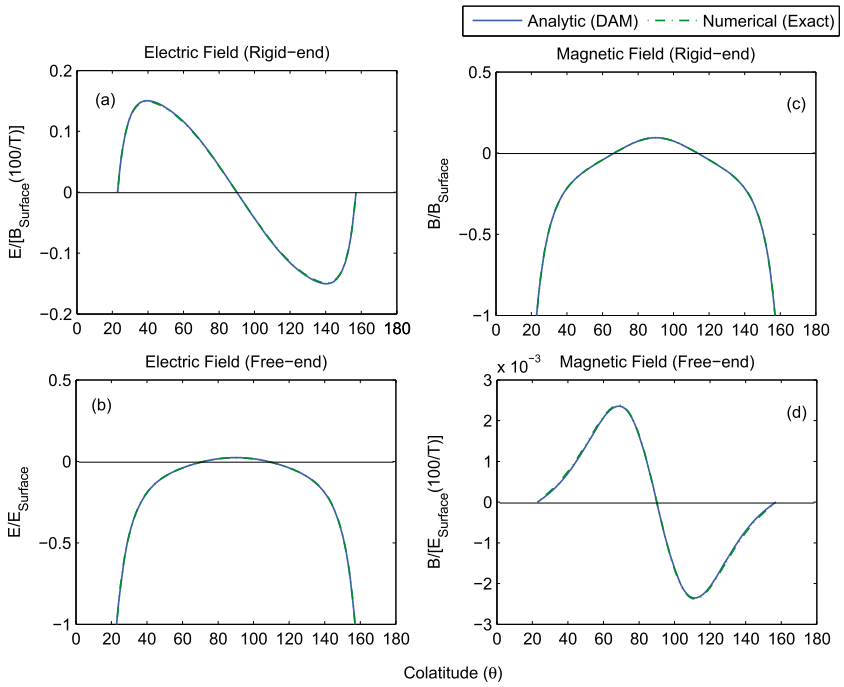

Figure 4. Same as Figure 3 but for second harmonic.

For this purpose, we used the frequencies observed by *Menk et al.* [1999] and *Takahashi et al.* [2002, 2004]. The observed frequencies cover all MLT sectors for L values ranging from 3 to 9. However, we consider only those events which lie in 0800–1600 MLT hours believing that Rigid-end condition is relevant to this range of MLT only. We pick up pulsation frequencies during quiet geomagnetic conditions ($k_P = 0 - 2_0$) as the present model best describes the field line characteristics during quiet geomagnetic conditions. It should be noted that the model has the potential to account for disturbed geomagnetic conditions as well [*Sinha and Rajaram*, 2003].

For any reported frequency f_{observed}, corresponding to a particular L shell, the equatorial ion number density ($n0$) (assuming protons as the only ion species) was computed using our model. Theoretical estimates of frequencies f_{model} were computed for a range of $n0$ such that $|f_{\text{model}} - f_{\text{observed}}| < \delta f$, where δf is the error in the frequency estimate. In our analysis, δf is considered as 0.01. The resulting error in density δn can be estimated as $\left(\frac{\partial n}{\partial f}\right)_{f_{\text{observed}}} \delta f$. This technique is applied to each of the methods DAM, NES, and WKB to obtain the analytic, numerical, and WKB estimates of $n0$ assuming both Rigid-end and Free-end conditions.

5.1. Variation With Respect to *L* shell

Figure 5 shows the estimates of equatorial ion densities obtained using all three methods discussed above under Rigid-end and Free-end boundary conditions. For the estimated $n0$, the superscripts R and F refer to estimates under Rigid-end and Free-end boundary conditions, respectively, and the subscripts DAM, NES, and WKB denote the respective methods employed. In all figures, frequencies are considered for L shells ranging between 3 and 9 and densities are estimated for indices $m = 0$–5 as all the estimates are concurrent for $m = 6$. The following inferences can be drawn from this figure. (a) The estimates of $n0$ using Free-end ($n0^F_{\text{NES}}$ or $n0^F_{\text{DAM}}$) lie above WKB estimates ($n0_{\text{WKB}}$) and that for Rigid-end ($n0^R_{\text{NES}}$ or $n0^R_{\text{DAM}}$) lie below it. (b) The analytic estimates of densities for both Rigid-end and Free-end ($n0^R_{\text{DAM}}$, $n0^F_{\text{DAM}}$) are slightly higher than corresponding numerical estimates of densities ($n0^R_{\text{NES}}$, $n0^F_{\text{NES}}$). (c) The departure in density estimates reduces with increasing density index m and for $m = 6$, the density computed from all these methods become equal (not shown here). (d) Irrespective of the method used, a consistent sudden decrease of plasma density is evident for all density indices between L shells 5 and 6. This marks the location of plasmapause across which the cold, dense plasma of plasmasphere shows a sudden decrease in the number density (shown as vertical grey area). The background for the pulsation events used in this study were quiet ($kp = 0$–2). Under such conditions, the location of plasmapause lies between $L = 5$ and 6 during day and night conditions [*Moldwin et al.*, 2002; *O'Brien and Moldwin*, 2003]. Therefore, under quiet geomagnetic conditions the location of plasmapause from our model

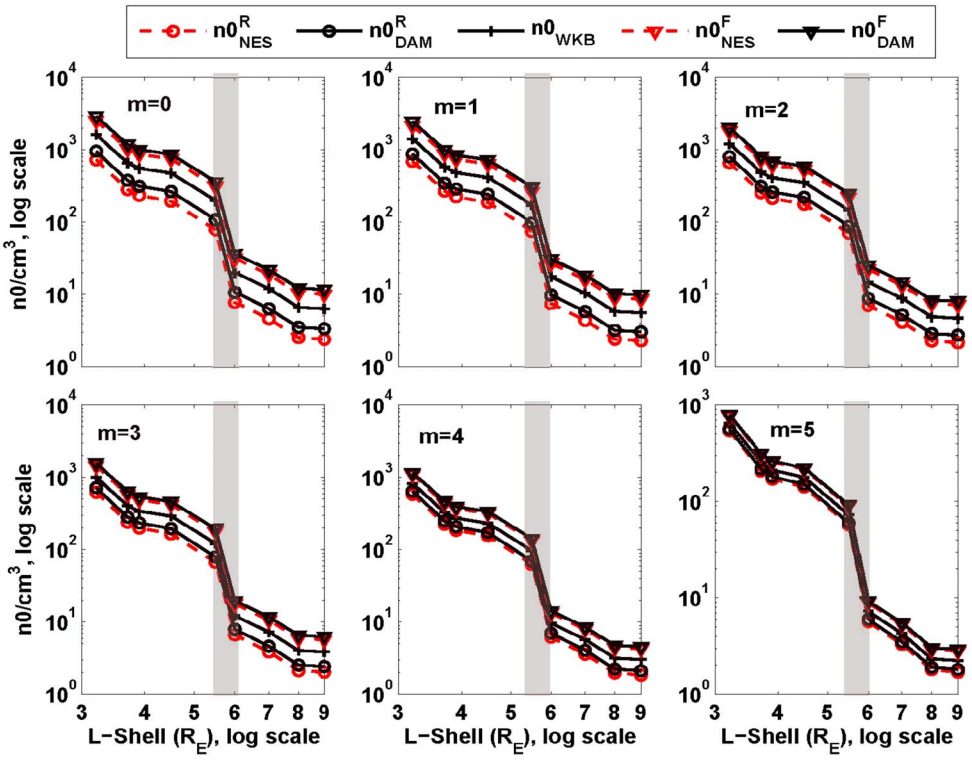

Figure 5. Variation of equatorial ion number density estimated using NES, DAM, and WKB with density indices under Rigid-end and Free-end boundary conditions for *L* shells ranging from 3 to 9. The parameter *n*0 denotes the equatorial ion number density. Both *n*0 and *L* are expressed in log scale. Superscripts *R* and *F* represent the Rigid-end and Free-end conditions. Subscripts DAM, NES, and WKB denote the respective methods used in computing the ion number densities. Each panel denotes the variation of *n*0 with *L*, for a given density variation. Vertical grey area denotes the location of plasmapause.

is consistent with earlier observational results. This emphasizes that the observed pulsations can be used in the developed theoretical model to estimate the magnetospheric plasma density.

5.2. Variation With Respect to Density Index *m*

The variation of equatorial ion number density (*n*0) with density indices *m* from all the three methods, viz., DAM, NES, and WKB are shown in Figure 6. The panels of Figure 6 depict this variation for different *L* shells between 3 and 9. A remarkable feature to be noted here is that for a given *L* value, the equatorial ion number density decreases linearly with density index *m*. Also, for a given *m*, the said density is lower for higher *L* values, which is also evident from Figure 5. For a particular *L* and *m*, number density evaluated through DAM shows better agreement with that computed through NES, whereas the number density computed using WKB shows large departure for the same *L* and *m* values.

5.3. Day-Night Comparison

Since pulsation events can occur in different MLT sectors, thus, the ionospheric conditions used need to be incorporated accordingly. For example, for events during daytime, Rigid-end, and for the events at night, Free-end, boundary conditions should be used. Irrespective of occurrence time of pulsations, it is customary to use Rigid-end conditions while estimating the equatorial ion number densities [*Menk et al.*, 1999; *Denton et al.*, 2001, 2004; *Takahashi and Denton*, 2007; *Menk and Waters*, 2013]. In order to address the departure in densities using two extreme ionospheric conditions, we examine the ratios of equatorial ion number densities obtained from Rigid-end and Free-end conditions.

Figure 7 presents the comparison of the equatorial ion densities obtained using the three methods discussed above under Rigid-end and Free-end boundary conditions. The parameters have the same meaning as in Figure 5. The ratio of equatorial ion number density computed from NES under Free-end condition ($n0^F_{NES}$) to that computed under Rigid-end condition ($n0^R_{NES}$) is shown in Figure 7a. The same using DAM has been shown

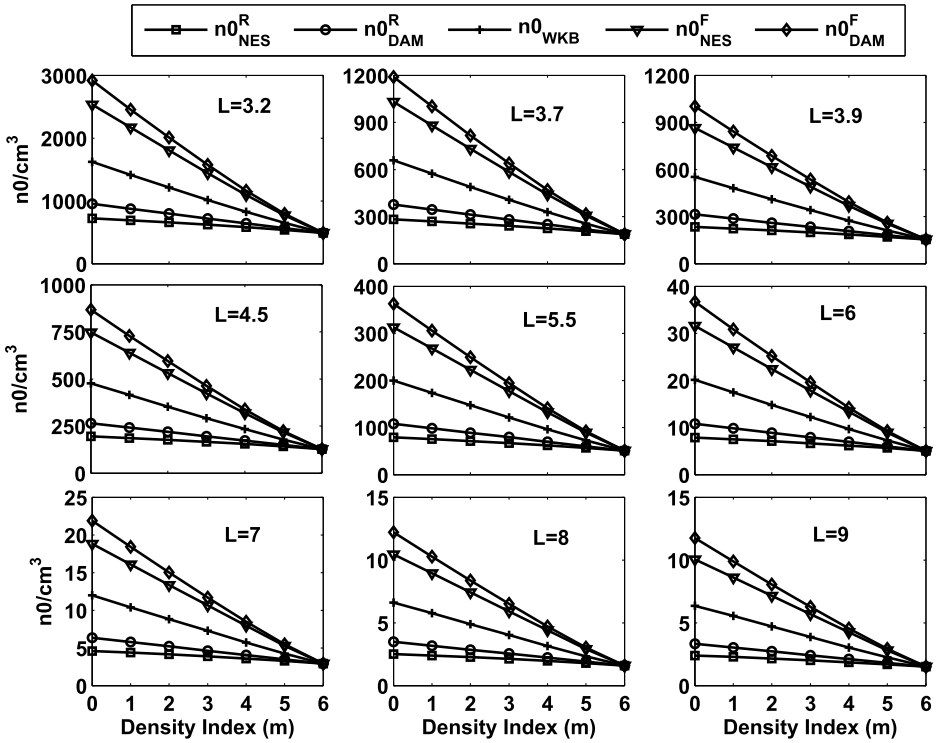

Figure 6. Variation of equatorial ion number density with density indices estimated using NES, DAM, and WKB under Rigid-end and Free-end boundary conditions for *L* shells 3 to 9. The parameters have the same meaning as in Figure 5.

in Figure 7b. It is clearly evident that the use of Free-end boundary condition instead of Rigid-end condition overestimates the equatorial ion number density if the event occurs during daytime. This ratio increases with *L* and decreases with *m*. The ratio shows identical features using DAM as well (Figure 7b). In fact, this ratio could be as large as 4 (Figure 7) which emphasizes the importance of ionospheric boundary condition.

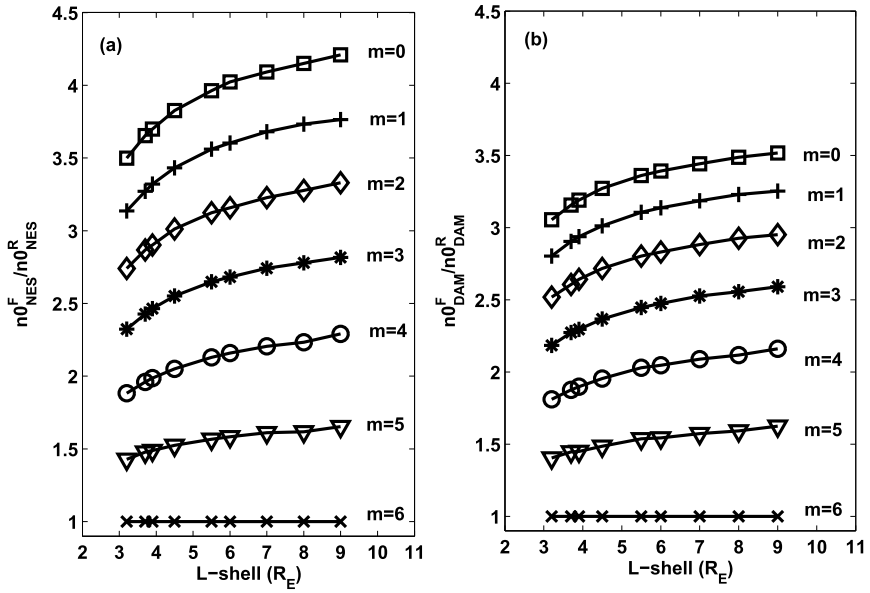

Figure 7. Day-night asymmetry in variation of ratio of equatorial ion number density estimated for *L* shells ranging between 3 and 9 and for range of density indices *m* = 0–6 using NES and DAM, respectively. The parameters have the same meaning as in Figure 5.

Table 3. Departure in Density Estimates Obtained Using Free-End From That Obtained Using Rigid-End for Density Indices m = 0–6 and Typical L Shells Using NES and DAM

L (R_E)	Density Index (m)	NES $(n0^F_{NES} - n0^R_{NES})$(/cm^3)	DAM $(n0^F_{DAM} - n0^R_{DAM})$(/cm^3)
	6	0	0
	5	231	238
	4	514	520
3.2	3	822.5	853
	2	1146.5	1212
	1	1478	1579
	0	1809	1962
	6	0	0
	5	2.01	2.0
	4	4.3	4.4
7	3	6.8	7.06
	2	9.2	9.8
	1	11.7	12.6
	0	14.22	15.5
	6	0	0
	5	1.11	1.13
	4	2.4	2.5
8	3	3.8	4.0
	2	5.2	5.5
	1	6.6	7.09
	0	7.94	8.7
	6	0	0
	5	1.1	1.1
	4	2.4	2.45
9	3	3.7	3.85
	2	5.0	5.3
	1	6.33	6.85
	0	7.67	8.41

The departure in density estimates under Free-end and Rigid-end cases is shown in Table-3 which presents difference of densities $(n0^F_{NES} - n0^R_{NES})$, estimated using NES and $(n0^F_{DAM} - n0^R_{DAM})$, estimated using DAM for different L shells and range of density indices m = 0–6. It can be clearly seen that for m = 6, there is no departure between densities estimated using Free-end or Rigid-end condition for any L shell. However, with decreasing m, the departure of density estimates increase and is maximum for m = 0. In addition, this departure is more for lower L shells. This shows that suitable boundary condition is very important for correct estimation of densities and becomes highly crucial for lower L shells. Density departure between Rigid-end and Free-end cases are in good agreement for both methods, i.e., NES and DAM.

Ozeke and Mann [2005] have addressed the effect of various ionospheric conditions and estimated the error if appropriate boundary conditions are not used. Their numerical estimates could address these errors for all density indices (m = 0–6). However, the analytic estimates were restricted only to $1/r^6$ type density variation. They suggested WKB method as possible analytic model that can be used to compute the densities for m other than 6. From Table 2, it is clearly evident that WKB frequencies show significant departure as compared to the NES frequencies for all m values apart form 6. Moreover, the WKB approach, based on time of flight computation, does not distinguish between Rigid-end and Free-end boundary conditions and hence cannot

account for day-night asymmetry. This discrepancy in frequency is bound to be reflected in the estimates of magnetospheric plasma density as well.

Interestingly, the ratio of density from all these methods is 1 for a density index $m = 6$. This is because for density variation of $1/r^6$ ($m = 6$), the term $\Phi(v)$ is only Ω^2 and equation (4) reduces to simple harmonic type whose solutions are straightforward and identical as obtained through DAM, NES, and WKB under both Rigid-end and Free-end cases. This means that for regions of the magnetosphere where plasma density follows a $1/r^6$-type variation along the field line, the equatorial ion number density can be estimated using any of the methods, viz., NES, DAM, and WKB under Rigid-end or Free-end boundary condition. Different regions of magnetosphere are characterized by different density profiles along the field line. Hence, there is a need for a suitable model that can estimate the plasma density with minimum error. The estimates of ion number density from DAM is very close to that estimated through NES for all the density indices under Rigid-end condition. This ratio is maximum for $m = 0$ (~1.4 times for Rigid-end and ~1.15 times for Free-end at typical $L = 6$). While using WKB approach, these ratios are, respectively, 2.6 and 0.63 for Rigid-end and Free-end for the same L shell. Thus, DAM shows remarkable improvement over earlier analytic model [*Ozeke and Mann*, 2005] which were valid only for $1/r^6$-type density distribution. This is tantamount to saying that the application of suitable boundary condition relevant to different MLT conditions while estimating equatorial ion number density is very crucial. To demonstrate the implication of boundary condition in computing the normal modes, it has been shown that for dawn and dusk MLT sectors, where the ionospheric conductivities are highly asymmetric, quarter wave modes are generated [*Allan and Knox*, 1979a; *Bulusu et al.*, 2014].

Although the illustration presented here is for events during daytime MLT hours, the analysis is applicable for night MLT hours as well. A similar contrast of densities would be observed between the Free-end (events occurring during night MLT hours) and Rigid-end (events during MLT hours) boundaries. Therefore, application of suitable boundary condition is essential while computing the ion densities. Once $n0$ is known, the ion number density in any region of magnetosphere and at any point along the field line can be realized using the appropriate density profile characterized by m value.

In this paper, we have developed a comprehensive model that accounts for toroidal oscillations during both Rigid-end (day) and Free-end (night) conditions. For this purpose, analytic (DAM), numerical (NES), and WKB (WKB) methods are worked out in the background dipole magnetic field geometry. It has been seen that DAM provides better agreement over WKB when compared to corresponding NES model. However, there are certain limitations in the developed model. First and foremost, the solutions are obtained for idealistic boundary conditions (Rigid end: infinitely conducting ionosphere; Free-end: vanishingly small ionospheric conductivity). Idealistic ionospheric condition cannot account for the damping at the conjugate point. The rates of damping are different for day and night hours. *Newton et al.* [1978] have demonstrated that the damping during nighttime is 50 times more as compared to that during daytime. That is why continuous pulsations are observed predominantly in the dayside. Thus, care must be taken in applying this model while estimating magnetospheric plasma densities.

Second, the applicability of the developed model for observations in the nightside auroral latitudes is of critical importance. During nighttime, the particle precipitation at auroral latitudes ($L > 6$) is significant. This leads to pronounced ionospheric conductivity at these latitudes. Thus, at high and auroral latitudes the Rigid-end condition is more applicable instead of the Free-end, even during nighttime.

The assumption of dipole magnetic field, as considered in the present model, may not be valid at higher L shells (L ~8–9). *Takahashi et al.* [2013] suggested a method as to how one can account for nondipole ambient field using the actual measurement. A better estimate of the mode frequency can be obtained by multiplying the theoretically estimated frequency with the magnetic field ratio ($\sim B_{\mathrm{Obs}}/B_{\mathrm{Dipole}}$) and obtain a corrected frequency a priori. Here B_{Obs} is the observed magnetic field and B_{Dipole} denotes the dipole magnetic field at the equator. While computing plasma densities, this factor must be taken into account.

In order to compute plasma density using pulsations, the frequencies need to be identified with least error. An observed quasi-monochromatic oscillation need not be due to a resonance mechanism. In order to categorize a particular pulsation event as a resonant oscillation, it is important to investigate the amplitude and phase variation of the observed frequency with latitude. *Baransky et al.* [1985] have illustrated the methodology to identify the resonant frequency at a particular latitude. A resonance signature of pulsation frequency is characterized by the amplitude maximum and phase reversal around the resonant latitude.

Irrespective of the limitations as discussed above, the present model provides qualitative results like day to night contrast in toroidal oscillation frequencies and corresponding signatures in the field parameters associated with the mode. We have demonstrated the applicability of the developed model to obtain the plasma density in the region where the pulsations are observed. The model gives a handle to experimentalists while evaluating and interpreting plasma densities in different ionospheric boundary conditions.

6. Concluding Remarks

In this paper, we give a comparative account of our model DAM with respect to standard WKB as well as exact NES solutions for Rigid-end and Free-end cases of half-wave toroidal oscillations. The study brings out that the mode frequency using DAM shows a remarkable improvement over standard WKB method. At geostationary height ($L = 6.6$), for the worst case of density index (i.e., $m = 0$, when the effect of singularity is maximum on the solution), the percentage departure of the DAM frequency from NES frequency for Rigid-end case is less than 17% and that from WKB is 60%. These departures of mode frequency for Free-end case are respectively 7% and 26% (cf. Tables 1 and 2). Proper handling of singularity at turning points is the key to this marked improvement. However, for higher harmonics, it is seen that frequencies obtained from DAM match very well with those obtained from NES method. Although in the Free-end case, the DAM frequency is off by 7% from NES frequency for the fundamental for $m = 0$ at $L = 6.6$, we note that the field-aligned structures obtained using DAM match quite well with the corresponding numerical exact solution (not shown in this paper). Though the spatial characteristics are shown only for a typical case of $m = 4$ at $L = 6.6$ (Figures 3 and 4), the electric and magnetic fields associated with toroidal half waves can be realized for any L shell and generalized plasma density variation characterized by m value.

More importantly, we address the technique for estimating the equatorial ion number density using observed frequencies in all the three methods (DAM, NES, and WKB) for the two idealistic boundary conditions, viz., Rigid-end and Free-end cases. This is important as the pulsation events can be observed in any MLT sectors characterized by different field-aligned density profile and ionospheric boundary conditions. The detailed analysis from all these methods clearly shows that the estimates of ion number density using DAM is more reliable as compared to WKB solution when compared to corresponding ion umber density obtained using NES. Earlier analytic models for computing the equatorial ion number density were restricted only to $1/r^6$-type density variation along the field line. The present study provides a working analytic model (DAM) to estimate the ion number density in different magnetospheric regions using observed ULFs in that region.

Acknowledgments
Data are available upon request from the corresponding author. We are thankful to Nadezda Yagova and the other referee for their constructive suggestions which helped in improving the quality of the manuscript.

Alan Rodger thanks Pavel Mager and another reviewer for their assistance in evaluating this paper.

References

Allan, W. (1983), Quarter-wave ULF pulsations, *Planet. Space Sci.*, *31*, 323–330, doi:10.1016/0032-0633(83)90083-1.

Allan, W., and F. B. Knox (1979a), A dipole field model for axisymmetric Alfvén wave with finite ionospheric conductivities, *Planet. Space Sci.*, *27*, 79–85.

Allan, W., and F. B. Knox (1979b), The effect of finite ionospheric conductivities on axisymmetric toroidal Alfvén wave resonances, *Planet. Space Sci.*, *27*, 939–950.

Anderson, B. J., M. J. Engebretson, S. P. Rounds, L. J. Zanetti, and T. A. Potemra (1990), A statistical study of Pc3–5 pulsations observed by the AMPTE/CCE magnetic fields experiment 1. Occurrence distributions, *J. Geophys. Res.*, *95*, 10,495–10,523.

Baransky, L. N., Yu. E. Borovkov, M. B. Gochberg, S. M. Krylov, and V. A. Troitskaya (1985), High resolution method of direct measurement of the magnetic field-lines eigenfrequencies, *Planet. Space Sci.*, *33*, 1369–1374.

Berube, D., M. B. Moldwin, and M. Ahn (2006), Computing magnetospheric mass density from field line resonances in a realistic magnetic field geometry, *J. Geophys. Res.*, *111*, A08206, doi:10.1029/2005JA011450.

Bochev, A. Z., and A. K. Sinha (2010), A coordinated study of field-aligned currents and Pc5 ULF waves during ejecta 1997, *Adv. Space Res.*, *46*, 1111–1119.

Bulusu, J., A. K. Sinha, and G. Vichare (2014), Toroidal quarter waves in the Earth's magnetosphere: Theoretical studies, *Astrophys. Space Sci.*, *353*, 395–404, doi:10.1007/s10509-014-2052-2.

Carpenter, D. L., and R. L. Smith (1964), Whistler measurements of electron density in the magnetosphere, *Rev. Geophys.*, *71*, 415–441.

Chi, P. J., and C. T. Russell (2005), Travel-time magnetoseismology: Magnetospheric sounding by timing the tremor in space, *Geophys. Res. Lett.*, *32*, L18108, doi:10.1029/2005GL023441.

Cummings, W. D., R. J. O'Sullivan, and P. J. Coleman (1969), Standing Alfvén waves in the magnetosphere, *J. Geophys. Res.*, *74*, 778–793.

Denton, R. E., M. R. Lessard, R. Anderson, E. G. Miftakhova, and J. W. Hughes (2001), Determining the mass density along magnetic field lines from toroidal eigenfrequencies: Polynomial expansion applied to CRRES data, *J. Geophys. Res.*, *106*(A12), 29,915–29,924.

Denton, R. E., K. Takahashi, R. R. Anderson, and M. P. Wuest (2004), Magnetospheric toroidal Alfvén wave harmonics and the field line distribution of mass density, *J. Geophys. Res.*, *109*, A06202, doi:10.1029/2003JA010201.

Dungey, J. W. (1954), Electrodynamics of the outer atmospheres, *Rep. 69*, Ions. Res. Lab. Pa. State Univ., University Park.

Dungey, J. W. (1968), Hydromagnetic waves, in *Physics of geomagnetic phenomena*, edited by S. Matsushita and W. Campbell, pp. 913, Academic Press, New York.

Engebretson, M. J., L. J. Zanetti, T. A. Potemraa, and M. H. Acufia (1986), Harmonically structured ULF pulsations observed by AMPTE/CCE magnetic field experiment, *Geophys. Res. Lett.*, *13*, 905–908.

Fedorov, E. N., B. N. Belenkaya, M. B. Gokhberg, S. P. Belokris, L. N. Baransky, and C. A. Green (1990), Magnetospheric plasma density diagnosis from gradient measurements of geomagnetic pulsations, *Planet. Space Sci.*, *38*, 269–272.

Gallagher, D. L., P. D. Craven, and R. H. Comfort (2000), Global core plasma model, *J. Geophys. Res.*, *105*, 18,819–18,833.

Goldstein, J., R. E. Denton, M. K. Hudson, E. G. Miftakhova, S. L. Young, J. Menietti, and D. Gallagher (2001), Latitudinal density dependence of magnetic field lines inferred from Polar plasma wave data, *J. Geophys. Res.*, *106*, 6195–6201.

Guglielmi, A. V. (1974), Diagnostics of the magnetosphere and interplanetary medium by means of pulsations, *Space Sci. Rev.*, *16*, 331–345.

Guglielmi, A. V. (1989), Diagnostics of the plasma in the magnetosphere by means of measurement of the spectrum of Alfvén oscillations, *Planet. Space Sci.*, *37*, 1011–1012.

Hughes, W. J., and D. J. Southwood (1976), The screening of micropulsation signals by the atmosphere and ionosphere, *J. Geophys. Res.*, *81*, 3234–3240.

Klimushkin, D. Yu., P. N. Mager, and K.-H. Glassmeier (2004), Toroidal and poloidal Alfvén waves with arbitrary azimuthal wave numbers in a finite pressure plasma in the Earth's magnetosphere, *Ann. Geophys.*, *22*, 267–287.

Krylov, A. L., and E. N. Fedorov (1976), Concerning eigen oscillations of bounded volume of a cold magnetzed plasma, *Dokl. Akad. Nauk SSSR*, *231*, 68–70.

Krylov, A. L., and A. E. Lifshitz (1984), Quasi-Alfvén oscillations of magnetic surfaces, *Planet. Space Sci.*, *32*, 481–492.

Krylov, A. L., A. E. Lifshitz, and E. N. Fedorov (1979), On the plasma resonances in a curvelinear magnetic field, *Dokl. Akad. Nauk SSSR*, *247*, 1095.

Krylov, A. L., A. E. Lifshitz, and E. N. Fedorov (1980), About resonant properties of the magnetospheric field-lines, *Geomag. Aeron.*, *20*, 689.

Langer, R. E. (1949), The asymptotic solutions of ordinary linear differential equations of second order, with special reference to a turning point, *Trans. Am. Math. Soc.*, *67*, 461–490.

Lanzerotti, L. J., and D. J. Southwood (1979), Hydromagnetic waves, in *Solar System Plasma Physics, III*, edited by L. J. Lanzerotti, C. F. Kennel, and E. N. Parker, pp. III, North-Holland, Amsterdam.

Leonovich, A. S. (2001), A theory of field line resonance in a dipole-like axisymmetric magnetosphere, *J. Geophys. Res.*, *106*, 25,803–25,812.

Leonovich, A. S., and V. A. Mazur (1993), A theory of transverse small-scale standing Alfvén waves in an axially symmetric magnetosphere, *Planet. Space Sci.*, *41*, 697–717.

Liu, W., J. B. Cao, X. Li, T. E. Sarris, Q.-G. Zong, M. Hartinger, K. Takahashi, H. Zhang, Q. Q. Shi, and V. Angelopoulos (2013), Poloidal ULF wave observed in the plasmasphere boundary layer, *J. Geophys. Res. Space Physics*, *118*, 4298–4307, doi:10.1002/jgra.50427.

Mager, P. N., and D. Yu. Klimushkin (2006), On impulse excitation of the global poloidal modes in the magnetosphere, *Ann. Geophys.*, *24*, 2429–2433.

Mager, P. N., and D. Yu. Klimushkin (2007), Generation of Alfvén waves by a plasma inhomogeneity moving in the Earth's magnetosphere, *Plasma Phys. Rep.*, *33*, 391.

Mann, I. R., and A. N. Wright (1995), Finite lifetimes of ideal poloidal Alfvén waves, *J. Geophys. Res.*, *100*, 23,677–23,686.

McClay, J. F. (1970), On the resonant modes of a cavity and the dynamical properties of micropulsations, *Planet. Space Sci.*, *18*, 1673–1690.

Mead, G. D., and D. H. Fairfield (1975), A quantitative magnetospheric model derived from spacecraft magnetometer data, *J. Geophys. Res.*, *80*, 523–534.

Menk, F. W., and C. L. Waters (2013), *Magnetoseismology: Ground-Based Remote Sensing of Earth's Magnetospheree*, WILEY-VCH, Weinheim, Germany.

Menk, F. W., D. Orr, M. A. Clilverd, A. J. Smith, C. L. Waters, D. K. Milling, and B. J. Fraser (1999), Monitoring spatial and temporal variations in the dayside plasmasphere using geomagnetic field line resonances, *J. Geophys. Res.*, *104*, 19,955–19,969.

Min, K., J. Bortnik, R. E. Denton, K. Takahashi, J. Lee, and H. J. Singer (2013), Quiet time equatorial mass density distribution derived from AMPTE/CCE and GOES using the magnetoseismology technique, *J. Geophys. Res. Space Physics*, *118*, 6090–6105, doi:10.1002/jgra.50563.

Moldwin, M. B., L. Downward, H. K. Rassoul, R. Amin, and R. R. Anderson (2002), A new model of the location of the plasmapause: CRRES results, *J. Geophys. Res.*, *107*(A11), 1339, doi:10.1029/2001JA009211.

Newbury, I. T., R. H. Comfort, P. G. Richard, and C. R. Chappell (1989), Thermal He+ in the plasmasphere: Comparison of observations with numerical calculations, *J. Geophys. Res.*, *94*, 15,265–15,276.

Newton, R. S., D. J. Southwood, and W. J. Hughes (1978), Damping of geomagnetic pulsations by the ionosphere, *Planet. Space Sci.*, *26*, 201–209.

O'Brien, T. P., and M. B. Moldwin (2003), Empirical plasmapause models from magnetic indices, *Geophys. Res. Lett.*, *30*(4), 1152, doi:10.1029/2002GL016007.

Orr, D. (1973), Magnetic pulsations within the magnetosphere: A review, *J. Atmos. Terr. Phys.*, *35*, 1–2.

Orr, D., and J. A. D. Mathew (1971), The variation of geomagnetic micropulsation periods with latitude and the plasmapause, *Planet. Space Sci.*, *19*, 897–905.

Ozeke, L. G., and I. R. Mann (2005), High and low ionospheric conductivity standing guided Alfvén wave eigenfrequencies: A model for plasma density mapping, *J. Geophys. Res.*, *110*, A04215, doi:10.1029/2004JA010719.

Radoski, H. R. (1967), A note on oscillating field lines, *J. Geophys. Res.*, *72*, 418–419.

Scholer, M. (1970), On the motion of artificial ion clouds in the magnetosphere, *Planet. Space Sci.*, *18*, 977–1004.

Singer, H. J., D. J. Southwood, R. J. Walker, and M. G. Kivelson (1981), Alfvén wave resonances in a realistic magnetospheric magnetic field geometry, *J. Geophys. Res.*, *86*, 4589–4596.

Sinha, A. K., and R. Rajaram (1997), An analytic approach to toroidal eigen mode, *J. Geophys. Res.*, *102*, 17,649–17,657.

Sinha, A. K., and R. Rajaram (2003), Dominance of toroidal oscillations in dawn/dusk sectors: A consequence of solar wind pressure variation, *Earth Planets Space*, *55*, 93–104.

Sinha, A. K., T. K. Yeoman, J. AWild, D. M. Wright, S. W. H. Cowley, and A. Balogh (2005), Evidence of transverse magnetospheric field line oscillations as observed from Cluster and ground magnetometers, *Ann. Geophys.*, *23*, 919–929.

Southwood, D. J. (1974), Some features of field line resonances in the magnetosphere, *Planet. Space Sci.*, *22*, 483–491.

Southwood, D. J., and M. G. Kivelson (1990), The magnetohydrodynamic response of the magnetospheric cavity to changes in solar wind pressure, *J. Geophys. Res.*, *95*, 2301–2309.

Takahashi, K., and R. E. Denton (2007), Magnetospheric seismology using multiharmonic toroidal waves observed at geosynchronous orbit, *J. Geophys. Res.*, *112*, A05204, doi:10.1029/2006JA011709.

Takahashi, K., R. E. Denton, and D. Gallagher (2002), Toroidal wave frequency at $L = 6$–10: AMPTE/CCE observations and comparison with theoretical model, *J. Geophys. Res.*, *107*(A2), 1020, doi:10.1029/2001JA000197.

Takahashi, K., R. E. Denton, R. R. Anderson, and W. J. Hughes (2004), Frequencies of standing Alfvén wave harmonics and their implication for plasma mass distribution along geomagnetic field lines: Statistical analysis of CRRES data, *J. Geophys. Res.*, *109*, A08202, doi:10.1029/2003JA010345.

Takahashi, K., M. D. Hartinger, V. Angelopoulos, K.-H. Glassmeier, and H. J. Singer (2013), Multispacecraft observations of fundamental poloidal waves without ground magnetic signatures, *J. Geophys. Res. Space Physics*, *118*, 4319–4334, doi:10.1002/jgra.50405.

Warner, M. R., and D. Orr (1979), Time of flight calculations for high latitude geomagnetic pulsations, *Planet. Space Sci.*, *27*, 679–689.

Waters, C. L., R. L. Lysak, and M. D. Sciffer (2013), On the coupling of fast and shear Alfvén wave modes by the ionospheric Hall conductance waves in the magnetosphere, *Earth Planets Space*, *65*, 385–396.